Crosstalk between lattice-spin electron dynamics at spin textures and across multiple magnetic-electronic phases in La$_{1-x}$Sr$_x$MnO$_3$ ($x = 0.125, 0.175$)

Smrutiranjan Mekap,[1] Jeetendra Kumar Tiwari [ORCID],[2] Ajay Baro,[2] Tilak Das [ORCID],[1] Subhasis Ghosh [ORCID],[2] and Anushree Roy [ORCID][1]

[1]*Department of Physics, Indian Institute of Technology Kharagpur, Kharagpur 721302, India*
[2]*School of Physical Sciences, Jawaharlal Nehru University, New Delhi 110067, India*

Recently observed skyrmionic, bubble, stripelike spin textures, along with multiple possible magnetic and related electrical phases, have renewed interest in doped rare-earth perovskite material, lanthanum strontium manganite La$_{1-x}$Sr$_x$MnO$_3$ (LSMO). Microscopic mechanisms that lead to exotic spin dynamics, spin structures, and electrical transport of LSMO over the varied temperature range are still not well understood. In the present study, temperature-dependent micro-Raman spectroscopic measurements indicate the intriguing trend of the evolution of spin-phonon and electron-phonon couplings with temperature across multiple magnetic and electrical phases in LSMO ($x = 0.125, 0.175$) having orthorhombic and rhombohedral phases. Electrical transport and magnetization studies revealed a metal-insulator phase transition in LSMO-0.125, whereas the system remains in the metallic phase in LSMO-0.175 over the low-temperature ferromagnetically ordered state. The observed anomalous Raman spectral shifts across magnetic phase transition temperatures relate to the complex nature of the coupling between spin and phonon dynamics in these compounds. Especially, the systematic modulation in the change in Raman shift with temperature in the ferromagnetic metallic phase, over which these materials are expected to exhibit nearly zero-field stripe spin structure, is noteworthy. The onset of such a trend is observed just above the paramagnetic-to-ferromagnetic phase transition temperature in LSMO-0.125. The unusual variation of Raman spectral linewidth at the crossover between the insulating and metallic ferromagnetic phase in LSMO-0.125 indicates an intertwined electron density of states near Fermi energy and phonon dynamics at this juncture. To this end, we report the expected signature of the existence of orbital polaron in the ferromagnetic insulating phase of LSMO-0.125 by studying the detailed spectral profiles of high wave-number Raman modes under different excitation wavelengths and varying temperatures. Combined manifold spin-phonon coupling schemes and the existence of orbital polaron in the ferromagnetic insulating phase, as could be qualitatively deliberated from Raman measurements, offer a crucial ingredient for a better understanding of microscopic mechanisms for the formation of exotic phases and various spin textures in LSMO.

I. INTRODUCTION

Over the past decades, doped rare-earth perovskite lanthanum strontium manganite, La$_{1-x}$Sr$_x$MnO$_3$ (LSMO), attracted much attention due to the richness of interrelated charge, spin, lattice, and orbital degrees of freedom of the system. These classes of compounds display multiple electrical and magnetic phases, such as ferromagnetic metallic (FMM), ferromagnetic insulating (FMI), paramagnetic insulating (PMI), canted antiferromagnetism insulating (CAFM-I), and polaronic states [1–9]. The origin of colossal magnetoresistance (CMR) close to FMM-to-PMI transition has been extensively investigated [10–15]. Recently observed skyrmionic, bubble, stripe, and other spin textures [16–20] spawned new interest in these compounds. LSMO is considered as one of the most desired choices for spintronic applications because of its high spin polarization [21] and the high Curie temperature (T_C) [1] in the manganite perovskite family.

Studies on phonon dynamics shed light on the correlation between structural, magnetic, and electrical degrees of freedom of complex systems. Since the report on the detection of orbital wave in LaMnO$_3$ by Raman-scattering measurements [22], quite a few articles in the literature have discussed the origin of the FMI phase in orthorhombic LSMO by studying the high wave-number phonon modes, coupled with this elementary excitation of the system [23,24]. Self-trapped orbiton-mediated multiphonon scattering via the Franck-Condon process was predicted theoretically by Allen and Perebeinos [25–27]. In this process, first a self-trapped orbital defect (orbiton) is produced by the incident photon in the Jahn-Teller (JT) ground state. This excitation decays to orbital ground state via n-phonon resonant Raman scattering following the first-order electron-phonon interaction. Kruger *et al.* [28] attributed the observed Raman mode near 1300 cm^{-1} in LaMnO$_3$ to multiphonon Raman scattering via the Franck-Condon mechanism involving self-trapped orbitons formed in the JT state. Nonetheless, few reports [23,24] suggested that the above-mentioned Franck-Condon mechanism was insufficient to describe the multiphonon Raman modes in LSMO. The existence of orbital polaron in explaining the FMI phase of orthorhombic LSMO was predicted by studying the giant softening of the Mn-O breathing vibrational mode of LSMO [23]. The reports in the literature suggested that the orbiton-phonon coupling mechanism in LSMO was much stronger than expected in the Franck-Condon mechanism in LaMnO$_3$ [24]. In Ref. [24], the anomalous behavior of both Raman

214411-1
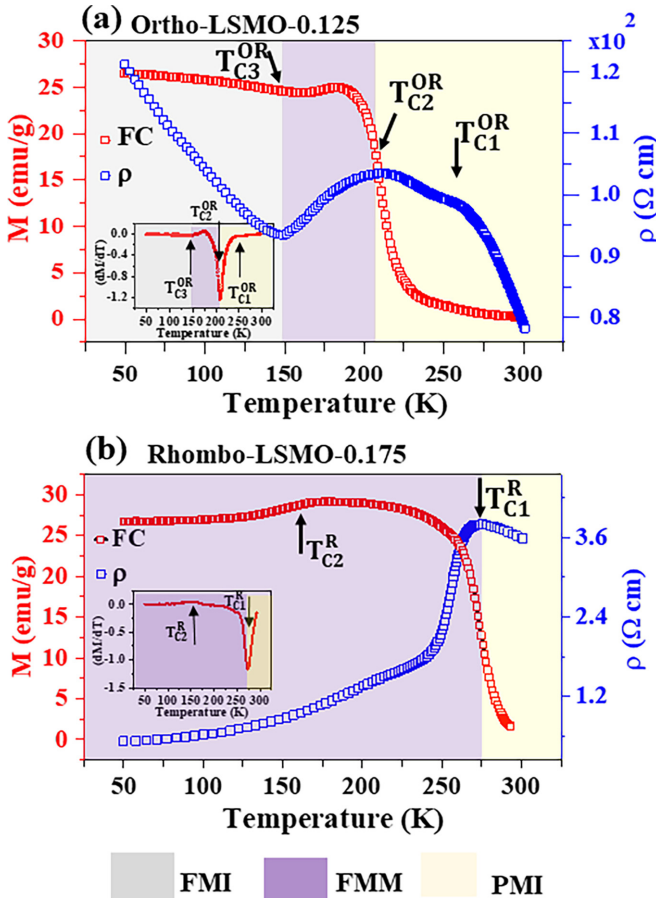
FIG. 1. Field-cooled magnetization (M) vs temperature (T) (in red) and resistivity (ρ) vs temperature (T) (in blue) plots for (a) LSMO-0.125 and (b) LSMO-0.175. The change in dM/dT with T is shown as an inset in each panel. T_C-s are marked by arrows in both panels.

shift and intensity of the higher wave-number Raman modes with temperature indicated the mixed orbiton-phonon character of the observed spectral feature in the FMI phase. It is to be noted that albeit innumerable studies on LSMO, reports on the evolution of spin-phonon coupling mechanism across multiple electrical and magnetic phases are still missing in the literature. Moreover, the lattice dynamics, while the system attains magnetic texture, is unexplored.

We choose La$_{0.875}$Sr$_{0.125}$MnO$_3$ (LSMO-0.125) and La$_{0.825}$Sr$_{0.175}$MnO$_3$ (LSMO-0.175) compounds having orthorhombic (O-LSMO) and rhombohedral (R-LSMO) crystal structures, respectively, for the present study as they show multiple phase transitions upon the change in temperature. Moreover, the crystal-field induce lattice distortion differs for these two structures, which further helps the present investigation. More importantly, both compounds exhibit stripe magnetic structures at relatively high temperatures and under nearly null magnetic fields [16–18]. The magnetization (M) and resistivity (ρ) vs temperature (T) plots of the compounds are shown in Fig. 1. Also, see the derivative of the M-T plot in the inset. In LSMO-0.125, while lowering the temperature, cooperative JT distortion in the PMI lattice sets in at T_{C1}^{OR} ($\sim$260 K). At $T_{C2}^{OR} \sim 210$ K, it attains an FMM phase. Below $T_{C3}^{OR} \sim 150$ K, the system becomes an insulator, retaining

the ferromagnetic phase (FMI). Details of the magnetization and electrical transport in this system are discussed elsewhere [29]. Reports in the literature [30–32] attribute T_{C3}^{OR} to charge ordering/orbital ordering transition, as the insulating state below this temperature arises due to the localization of charges and ordering of orbital. Figure 1(b) plots the change in magnetization and resistivity of LSMO-0.175 with temperature. The compound is in the PMI phase down to $T_{C1}^{R} \sim 274$ K, below which it attains an FMM phase. At T_{C2}^{R} ($\sim$167 K), the slight downturn of the magnetization plot is possibly related to the onset of a spin texture (stripes) in the FMM phase of the compound [8].

In this paper, we discuss the gradual evolution of spin-phonon coupling dynamics across the above-mentioned various magnetic and electrical phases of O-LSMO-0.125 and R-LSMO-0.175, using temperature-dependent micro-Raman spectroscopic measurements. The observed trends in spectral parameters can be correlated with the evolution of the magnetic and electric phases with temperature, suggesting the existence of manifold spin-phonon coupling mechanisms in the system. The unique undulation of the spectral parameters in the FMM phase (over which formation of stripe magnetic structures is reported) of both compounds suggests the existence of the intricate nature of different types of magnetic interactions in the system in this state and their tie with the lattice dynamics. A signature of strong electron-phonon coupling in LSMO-0.125 at the crossover between the FMI and the FMM phase is evident from the analysis of the thermal evolution of Raman linewidth. To this end, through a brief discussion on the high wave-number Raman-scattering measurements under varying excitation wavelengths over a wide range of temperatures, we reestablish the existence of orbital polaron to describe the FMI phase and its unrelatedness to JT distortion in O-LSMO-0.125. The finding has been further corroborated by the observations on R-LSMO-0.175, which do not exhibit the FMI phase.

II. EXPERIMENTAL DETAILS

LSMO-0.125 and LSMO-0.175 compounds were synthesized by standard solid-state reaction method [8,29]. The sample phase and purity were confirmed by x-ray-diffraction (XRD) measurements and reported elsewhere [8,29]. Rietveld refined XRD patterns of the compounds are available as Supplemental Material S1 in Ref. [33]. Micro-Raman measurements of the samples were carried out using the Raman spectrometer of model LabRam HR evolution (Horiba, France). The spectrometer was equipped with a confocal microscope (BX41, Olympus, Japan), a Peltier-cooled charge-coupled device detector (Syncerity, Horiba, USA), and a 532-nm Nd–yttrium aluminum garnet diode laser (Excelsior 532 single mode, Excelsior, UK) as the excitation source. With 1800 grooves per millimeter grating and 50-μm slit width, the resolution of the measurements was 0.5 cm^{-1}. The Raman spectra were also recorded using a 785-nm diode laser as the excitation source and a Raman spectrometer (IHR 550, Horiba, France). Temperature-dependent Raman spectra between 80 and 450 K were recorded using a low-temperature sample stage (model THMS600, Linkam, UK) equipped with a cryostat and a liquid nitrogen pump. All measurements were
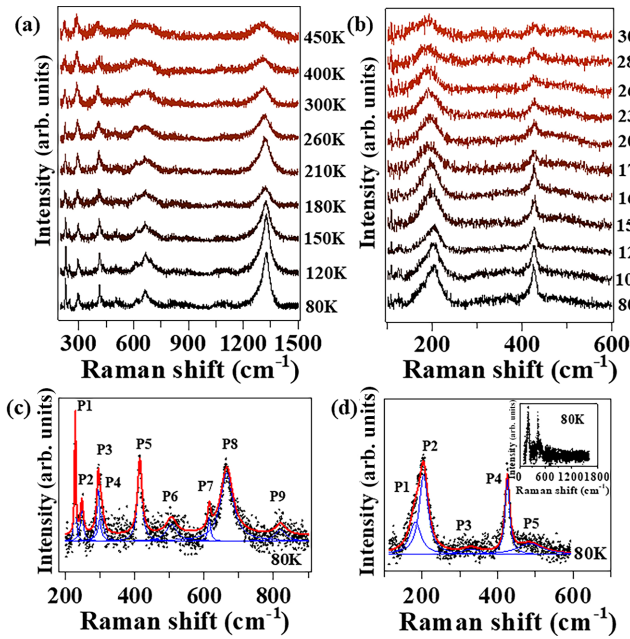
FIG. 2. Characteristic temperature-dependent Raman spectra of (a) O-LSMO-0.125 and (b) R-LSMO-0.175 at set temperatures, marked on the right. (c), (d) Recorded Raman spectra of LSMO-0.125 and LSMO-0.175, respectively, at 80 K. In each panel, the measured spectrum is shown by + symbols. Solid blue and red curves show the deconvoluted components and the net fitted spectrum, respectively. In (c), peaks P1–P9 and in (d) peaks P1–P5, discussed in the text, are marked. Inset of (d) plots the Raman spectrum of LSMO-0.175 over the spectral range between 100 and 1600 cm^{-1} at 80 K.

performed using an objective lens of magnification 50× to focus the laser beam on the sample and to collect the scattered light in the backscattered geometry.

Both samples were tested with different incident laser power and integration time to avoid laser heating. All reported data were recorded with 1-mW laser power on the sample. We observed a significant change in spectral profile for higher laser powers. Before the measurements, temperature stability was checked by recording the spectra after waiting at a set temperature for various times, varying from 2 to 30 min. We did not observe any spectral shift beyond 5 min of the waiting time. For all reported spectra, the waiting time was 10 min after attaining each set temperature.

III. RESULTS

Figures 2(a) and 2(b) plot characteristic Raman spectra of O-LSMO-0.125 and R-LSMO-0.175, respectively, at various temperatures. All temperature-dependent Raman spectra are available in Figs. S2(a) and S2(b). A large number of reports in the literature have discussed the first-order Raman modes of LSMO of different crystal structures [34–39]. For O-LSMO-0.125 with space group *Pbnm* (no. 62), group theory predicted 60 first-order gamma-point phonon modes, out of which 24 modes were Raman active following irreducible representation $\Gamma = 7A_g + 5B_{1g} + 7B_{2g} + 5B_{3g}$ [34]. The magnified view of the linear background-subtracted Raman spectrum recorded at 80 K over the spectral range between

200 and 900 cm^{-1} is shown in Fig. 2(c). We observed eight Raman modes (P1−P8) below 700 cm^{-1}. The Raman mode at 820 cm^{-1} (P9) was an overtone of the primary mode at P5. The spectrum was deconvoluted with a sum of nine Lorentzian functions, keeping the peak position, width, and intensity of each component as free-fitting parameters. The deconvoluted components and the net fitted spectrum are shown by blue and red solid curves, respectively. The atomic vibrations corresponding to observed modes P1–P7, using the results obtained from the calculations based on density-functional theory (DFT) on the LaMnO$_3$ bulk phase with space group *Pbnm*, are available as Supplemental Material Fig. S3(a) of Ref. [33]. In the simulation, we used the unit-cell volume of O-LSMO-0.125 (as obtained from the current Rietveld refinement of the XRD pattern) as the initial input. The details of the calculations are available as Supplemental Material S3 in Ref. [33], with Refs. [40–53]. The mode at 665 cm^{-1} could not be detected in the present DFT simulation. In the literature, this particular mode is assigned to the breathing mode of MnO$_6$ octahedra [28,39]. In Fig. 2(a), it is to be noted that the higher wave-number Raman modes beyond 1000 cm^{-1} are unexpectedly of higher intensity than that of first-order Raman lines. A discussion on these spectral features is available later in this paper.

The compound LSMO-0.175 with $R\bar{3}c$ (no. 167) space group has 30 gamma-point phonon modes, as predicted by group theory. Out of these 30 modes, 5 are Raman active, and the irreducible representations for Raman modes are given by $\Gamma = 1A_{1g} + 4E_g$ [38]. Raman spectrum recorded at 80 K, shown in Fig. 2(d), could be fitted with a sum of five Lorentzian functions. The deconvoluted components and net fitted spectrum are shown by the blue solid and red solid curves, respectively. The five observed Raman modes are marked as P1–P5 in Fig. 2(d). Similar broad modes for R-LSMO were reported earlier in the literature [38], the origin of which was assigned to the scattering by oxygen-related lattice vibration in the system. The schematic diagrams showing the atomic motion related to these Raman-active modes are available as Fig. S3(b) in Ref. [33], as obtained from the present DFT calculations of the parent compound LaMnO$_3$ with space group $R\bar{3}c$ (no. 161), having the unit-cell volume the same as the present compound LSMO-0.175. Though the relative intensity between the Raman peaks changed, we did not observe the appearance of any other new mode, indicating that the structural symmetry with space group *Pbnm* and $R\bar{3}c$ was retained in LSMO-0.125 and LSMO-0.175, respectively, over the entire temperature range of interest. Thus, all spectra recorded at various temperatures were analyzed as described for Figs. 2(c) and 2(d) for the corresponding phases. It is worth noting that unlike in LSMO-0.125, high wave-number Raman modes are absent for LSMO-0.175 [refer to the inset in Fig. 2(d)].

IV. DISCUSSION

A. Participation of phonon in multiple magnetic and electrical phase transitions

We direct the attention on intense first-order Raman modes, P1, P3, and P5, in Fig. 2(c). Figure 3(a) plots magnified spectra at different temperatures, focusing only on these
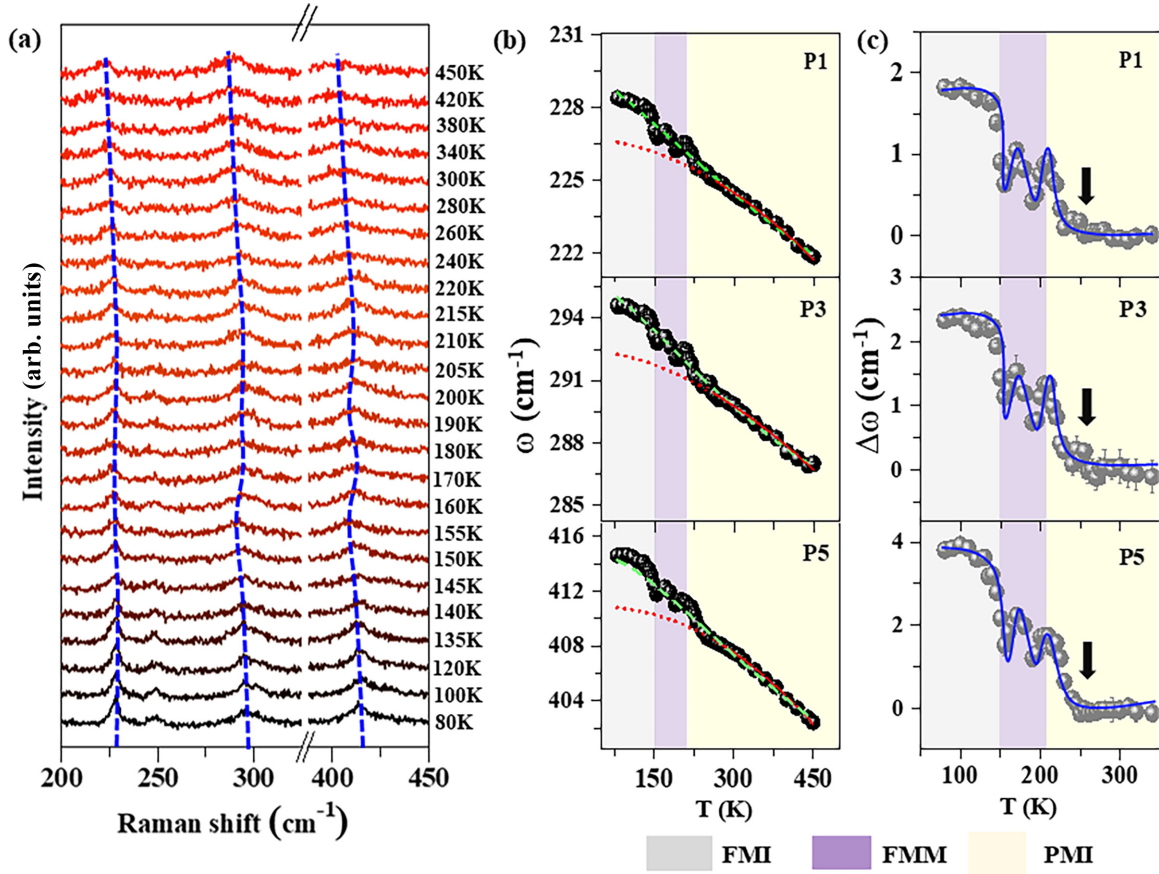
FIG. 3. (a) Magnified view of characteristic Raman spectra focusing on the evolution of P1, P3, and P5 with temperature of LSMO-0.125. The blue dashed lines mark the nonmonotonic shift in Raman wave number with temperature. (b) Evolution of Raman shifts with temperature for the peaks P1, P3, and P5. The error bars are the standard deviation of the parameters as obtained from the fitting procedure. Green dashed curves are the best fit to the data points over the entire temperature range of interest using Eq. (1). The solid red curves are best fit to the data points by the same equation for the temperature range $T > T_{C1}^{OR}$. These best-fitted solid red curves are extended up to 80 K and shown by dotted lines (see text). (c) Variation of $\Delta\omega$ [difference between values of the data point and the value on the red solid (extended) plot in (b)] with temperature. Blue solid curves are guides to the eyes. T_{C1}^{OR} in the PMI phase is marked by down black arrows. In (b) and (c), the yellow-, violet-, and gray-shaded areas in each panel mark the data points above T_{C2}^{OR}, between T_{C2}^{OR} and T_{C3}^{OR}, below T_{C3}^{OR}, respectively, following the color code in Fig. 1.

three intense Raman modes. The blue dashed lines mark the nonmonotonic Raman shift of the above three modes with temperature. The evolution of Raman shifts with temperatures of these modes, as obtained by following the above-mentioned curve-fitting procedure [for Fig. 2(c)] for spectra recorded at various temperatures, are shown in Fig. 3(b). According to Granado *et al.* [54], the temperature dependence of the change in phonon wave number in magnetic materials can be expressed by the following relation: $\omega(T) - \omega_0 = \Delta\omega_{latt} + \Delta\omega_{anh} + \Delta\omega_{sp} + \Delta\omega_{ren}$. ω_0 is the phonon frequency at 0 K, and $\Delta\omega_{latt}$ is the change in phonon frequency due to lattice expansion. The shift $\Delta\omega_{latt}$ can be estimated from the relative change in unit-cell volume ($\Delta V/V$) with temperature using the relation $\frac{\Delta\omega_j}{\omega} = -\gamma_j \frac{\Delta V}{V}$. $\Delta\omega_j$ is the shift in phonon frequency of the jth phonon mode, ω is the frequency of the jth phonon mode, and γ_j is the Grüneisen parameter of the jth mode. The value γ_j is ~2 for similar perovskites [55]. The change in unit-cell volume of LaMnO$_3$ between 80 and 300 K is only 0.4%, as obtained from small-angle neutron-scattering measurements [56]. Hence, the expected shift in Raman mode

due to the change in unit-cell volume is less than 1%. Thus, the contribution of the change in volume of the lattice over the temperature range of interest is negligible to account for the observed change in the Raman shift below T_{C1}^{OR} in Fig. 3(b).

$\Delta\omega_{anh}$ is the shift in the phonon frequency due to the anharmonic nature of the vibrational potential with the rise in temperature at the constant volume of the lattice. Considering three- and four-phonon decay processes in which one optical phonon decays into two and three acoustic phonon modes, the shift in the phonon wave number with temperature is given by [57]

$$\Delta\omega_{anh} = \omega_0 + \Delta(T), \text{ with}$$

$$\Delta(T) = A\left(1 + \frac{2}{e^{\phi/2} - 1}\right)$$
$$+ B\left(1 + \frac{3}{e^{\phi/3} - 1} + \frac{3}{(e^{\phi/3} - 1)^2}\right). \quad (1)$$

$\phi = \hbar\omega_0/k_B T$, and A, B are anharmonic constants corresponding to three- and four-phonon decay processes. k_B is

the Boltzmann constant. In addition, the spin-phonon coupling in a magnetically ordered system can shift phonon wave number ($\Delta\omega_{sp}$). $\Delta\omega_{ren}$ is the shift of phonon frequency as a result of the renormalization of electronic states near spin ordering temperature. We fit the variation of the ω vs T plot for the intense first-order Raman peaks P1, P3, and P5 in Fig. 3(b) for the whole temperature range using Eq. (1) and show by green dashed curves. For these phonon modes, the mismatch between the data points and fitted curves, especially in the low-temperature region, over which the system enters into different magnetically ordered states (shown by colored shaded areas: gray: FMI; violet: FMM; and yellow: PMI), is noteworthy.

To investigate the evolution of the Raman shift below T_{C1}^{OR}, we adopted the following procedure: It is to be recalled that above $T_{C1}^{OR} = 260$ K, the system is in the PMI phase, and the cooperative JT distortion in the system is yet to set in [32]. Thus, for $T > T_{C1}^{OR}$, the evolution of phonon wave number with temperature is governed by the anharmonicity of the vibrational potential only. In view of this, we fitted data points in Fig. 3(b) over the region $T > T_{C1}^{OR}$ with Eq. (1) [solid red curves in each panel of Fig. 3(b)]. Using the fitted parameters A and B (available as Supplemental Material S4 [33]), we generated the expected curves down to 80 K (dotted red curves), which carry the information of the evolution in Raman shifts with temperature only due to the change in anharmonicity in the system. The disparity between the data points and the extended dotted curves for each panel in Fig. 3(b) indicates that phonon wave numbers of the modes are affected by various other factors in addition to the anharmonicity in the low-temperature range.

The subtracted value on the fitted curve from the measured values of ω at the corresponding temperature, $\Delta\omega$ vs T plots in Fig. 3(c), provides a meaningful insight into the coupling lattice and spin degrees of freedom of the system across multiple phase transitions. As $\Delta\omega$ is ~ 0 for the entire temperature range above T_{C1}^{OR} when the system is in the PMI phase, for our subsequent discussion, we only show the data points related to the PMI phase up to 350 K in Fig. 3(c) so that the $\Delta\omega$ vs T plots below T_{C1}^{OR} could be magnified and followed in the panels with clarity. As in Fig. 3(b), the temperature ranges over which the system attains FMI, FMM, and PMI phases are shown by gray-, violet-, and yellow-shaded areas. As expected, beyond T_{C1}^{OR}, $\Delta\omega \approx 0$. Below T_{C1}^{OR}, the interesting nonmonotonic modulation of different natures in $\Delta\omega$ vs T plots is observed. For $T_{C1}^{OR} > T > T_{C2}^{OR}$, the increase in the value of $\Delta\omega$ [the yellow-shaded area in Fig. 3(c)] is due to the set-in of the cooperative JT distortion, which induces additional strain in the lattice over the same due to doping [9]. For $T_{C2}^{OR} > T > T_{C3}^{OR}$, we observe an interesting undulation in $\Delta\omega$ vs T plot, the onset of which occurred just above T_{C2}^{OR}. Here, we would like to mention that though the undulation is within the resolution (0.5 cm^{-1}) of our measurements, we have observed a similar trend for data points from three individual sets of measurements on the same sample (the results of another set of data are available in Supplemental Material Fig. S5 [33]). At T_{C2}^{OR} the system enters into the FMM state, i.e., both magnetic and electrical phases change. The value of $\Delta\omega$ begins to increase just below T_{C3}^{OR}, reaches a maximum at T_{C3}^{OR}, and then saturates. It is to be noted that

both in gray- and violet-shaded regions in Fig. 3(c), the system remains in the FM state; however, it undergoes metal-insulator transition (MIT) at T_{C3}^{OR}. The above observation possibly indicates the onset of different types of spin-phonon coupling schemes across FMM and FMI phases and/or renormalization of phonon frequency across MIT ($\Delta\omega_{ren}$ mentioned earlier).

The change in JT distortion across MIT can result in a change in the Raman shift [58]. As the system undergoes a transition to the FMM state, there is delocalization of the carrier, which reduces the distortion of MnO$_6$ octahedra and is expected to weaken the JT distortion. This may decrease the vibrational energy in the FMM state [58]. In the present system, the observed unchanged characteristics of JT distortion-related phonon mode below T_{C1}^{OR} (will be shown later) negates the above possible explanation as the origin of anomalous spin-phonon coupling across the FMI-FMM phase in this system.

Next, we look into the magnetoelastic coupling in LSMO-0.175. It is to be recalled that LSMO-0.175 is in the FMM phase below $T_{C1}^{R} \sim 274$ K, above which it turns into a PMI system. The magnified view of the evolution of intense peaks P2 and P4 is shown in Fig. 4(a). The blue dashed lines mark the change in peak positions with temperature. The evolution of Raman shift with temperature of the intense modes P2 and P4 [refer to Fig. 2(d)] are shown in Fig. 4(b). The data points are analyzed following the same methodology as discussed for Fig. 3(b) for LSMO-0.125. The dashed green curves are the best fits to the data points using Eq. (1), which determines the contribution of anharmonicity in the vibrational potential to the Raman shift with temperature. The mismatch between the fitted curve and data points in the low-temperature regime for peaks P2 and P4 prompted us to fit the data points above 274 K in the PMI phase using Eq. (1), shown by the red solid curve in Fig. 4(b). The extended curves till 80 K are shown by red dots. The evolution of $\Delta\omega$ with temperature, where $\Delta\omega$ is the difference between the values of the data point and the red dotted curves, is plotted in Fig. 4(c). The temperature ranges for FMM and PMI phases are marked as violet- and yellow-shaded areas, respectively. As in Fig. 3(c) for LSMO-0.125, above 274 K for the data points in PMI phase $\Delta\omega \approx 0$. We did not observe any appreciable changes in $\Delta\omega$ at the beginning of the FMM phase (in the violet-shaded area). However, like O-LSMO, an undulation was noted below T_{C2}^{R} (shown by open red arrows). Also see Fig. S5(b) in the Supplemental Material [33].

The unique oscillation-type $\Delta\omega$ vs T plots in Figs. 3(c) and 4(c) in the FMM phase over a particular temperature regime are noteworthy [also see Figs. S5(a) and S5(b) for a second set of data]. As mentioned earlier, in the literature, Lorentz transmission microscopy revealed the existence of magnetic stripe spin textures in various crystal planes of the FMM phase in LSMO-0.125 and below T_{C2}^{R} in LSMO-0.175 without an applied magnetic field [16–18]. Thus, the atypical modulation in $\Delta\omega$ vs T plots in Figs. 3(c) and 4(c) mentioned above possibly signifies a complex nature of spin-phonon coupling while magnetic textures are attained in the FMM phase.

For complex magnetic oxide systems, the stable magnetic phase is determined by elegant competitive interaction mech-
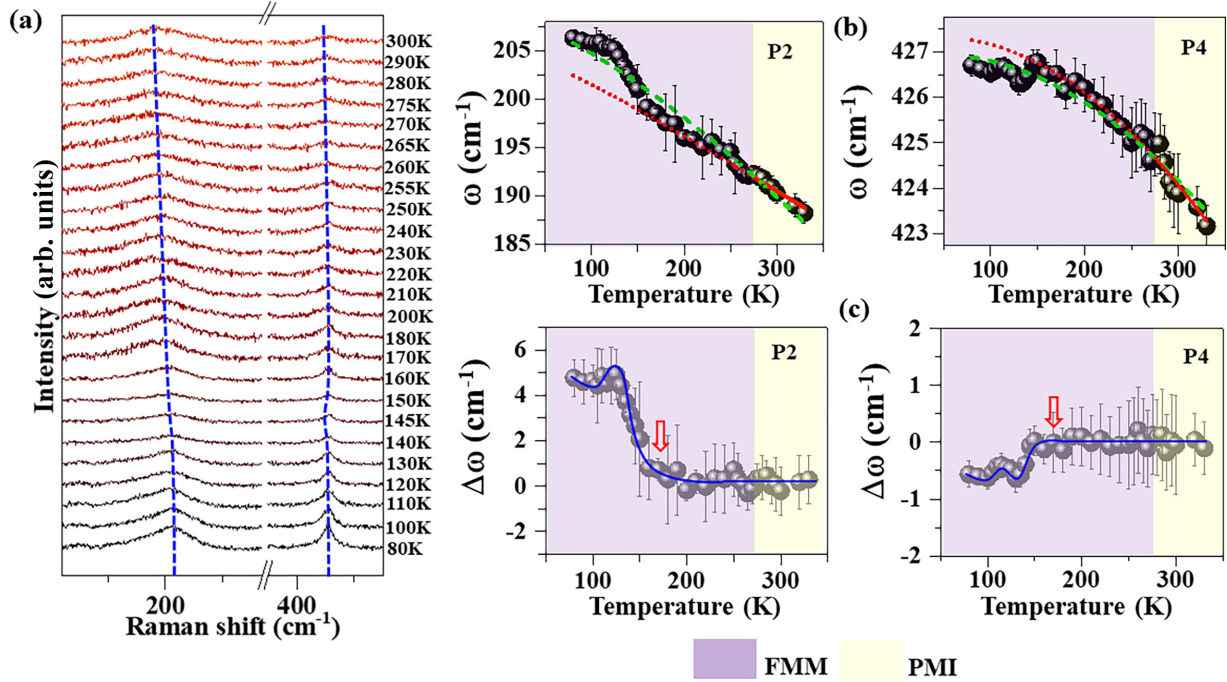
FIG. 4. (a) Magnified view of characteristic Raman spectra focusing on the evolution of P2 and P4 with temperature of LSMO-0.175. The blue dashed lines mark the nonmonotonic shift in Raman wave number with temperature. (b) Evolution of Raman shifts with temperature for the peaks P2 and P4. Green dashed curves are the best fit to the data points over the entire temperature range of interest using Eq. (1). The solid red curves are the best fit to the data points by the same equation for the temperature range $T > T_{C1}^{R}$. These best-fitted solid red curves are extended down to 80 K and shown by red dotted curves. (c) Variation of $\Delta\omega$ [difference between values of the data point and the value on the red fitted (extended) plot in (b)] with temperature. T_{C3}^{R} in the FMM phase is marked by red open arrows. Blue solid curves are guides to the eyes. In (b) and (c), the yellow-, and violet-shaded areas in each panel mark the data points between T_{C1}^{R} and T_{C2}^{R}, and below T_{C2}^{R}, respectively, following the color code in Fig. 1.

anisms following the spin-spin interaction Hamiltonian as [59] $H_{\text{spin}} = \sum_{ij}^{nn} [J_{\text{IE}}(\boldsymbol{S_i}.\boldsymbol{S_j}) + \boldsymbol{D_{ij}}.(\boldsymbol{S_i} \times \boldsymbol{S_j}) + \boldsymbol{S_i}. \Gamma_{ij}. \boldsymbol{S_j}] + A \sum (\boldsymbol{n_i}.\boldsymbol{S_i})^2$. While the first term corresponds to isotropic exchange (IE) interactions, the second, third, and fourth terms in the Hamiltonian correspond to the Dzyaloshinskii-Moriya (DM) interaction, anisotropic exchange (AE) interaction, and the single-ion anisotropy (SIA) interaction. J_{IE}, D_{ij}, and Γ_{ij} are IE, DM, and AE interaction coefficients. The SIA coefficient and the vector pointing in the direction of the easy axis are denoted by A and n, respectively. S_i and S_j are spin magnetic moments of the next-nearest neighbors. It is to be recalled that O-LSMO and R-LSMO have centrosymmetric crystal structures with space group $Pbnm$ and $R\bar{3}c$, respectively. DM interaction, in general, is observed in noncentrosymmetric magnetic materials [60,61]. However, quite a few reports in the literature suggested anisotropic spin-spin interaction in O-LSMO and R-LSMO [16–18]. Zhang *et al.* [20] have shown that the DM interaction can be achieved in a pseudocubic lattice of LSMO. The presence of relatively strong JT distortion (discussed later in this paper) and structural strain can result in local strain in the system [62,63], which can switch on the DM and other anisotropic spin-spin interactions in the doped system over a certain range of temperatures. A competing role of the above interaction mechanisms can result in a complex magnetoelastic coupling mechanism, leading to undulation in the $\Delta\omega$ vs T plot in the FMM phase. Here, we would like to mention that the oscillating magnetic field of an electromagnetic radiation can

induce an indirect magnetic dipole-dipole interaction [64]. However, such an effect of radiation is appreciable only under certain boundary conditions followed by dipole arrangements (permanent dipoles are at the edge) and under the resonance between the rotational frequency of the transition dipoles and the frequency of the magnetic field. Thus, it is unlikely that the observed undulation is due to any such effect of radiation on magnetic dipoles of the system and possibly arises only due to the cumulative effect of various types of direct spin-spin interactions mentioned above.

It is worth noting that though for all studied modes for LSMO-0.125 in Fig. 3(c), the nature of undulation, discussed above, is very similar for all three Raman modes, though P3 and P5 involve the atomic motion of MnO_6 octahedra, while P1 also involves atomic displacements of La/Sr. In contrast, for LSMO-0.175, an opposite trend (up and down of $\Delta\omega = 0$) for P2 and P4 is observed in Fig. 4(c), though both modes only involve the atomic motion of MnO_6 octahedra. Indeed, the role of difference in magnetocrystalline anisotropy for LSMO with different crystal symmetry governing magnetic textures has been discussed in the literature using Lorentz transmission microscopy [17]. Thus, it is reasonable to believe that the symmetry of the crystal structure determines the coupling mechanism of the electronic spin and lattice dynamics in the magnetic stripe phase of the compounds via anisotropic interactions. It is to be noted that the quantitative estimation of spin-phonon coupling strength over different magnetic and electrical phases of the compounds is nontrivial because of

the complex nature of spin-spin interaction in this system. The well-known formalism proposed by Grando *et al.* [54] for estimating spin-phonon coupling strength is valid only when the superexchange interaction following the Hamiltonian $H = J\langle\vec{S}_i.\vec{S}_j\rangle$ prevails. Hence, it cannot be exploited in the present study.

B. Signature of strong electron-phonon coupling across low-temperature FMM-FMI phase transition

Studies on the topology of Fermi surface and electrons–quasiparticle dynamics using angle-resolved photo emission spectroscopy (ARPES) measurements [65–71] indicate "nodal-antinodal dichotomy" via the formation of pseudogap at the antinode and quasiparticle (polaron) excitations at the nodal points of band dispersion in the FMM phase of LSMO, like in superconductors [66]. Detailed investigation of the 3D electronic structure using *in situ* high energy-resolution ARPES measurements showed a distinct kink near Fermi energy around Fermi momentum, which, in turn, suggested electronic-bosonic gluing in the system [71]. Inelastic neutron scattering further attributes the observed kink to strong electron-phonon coupling in the FMM phase of LSMO, which is suggested to be the genesis of polaronic quasiparticles [71].

The theory of thermal equilibrium of electronic density of states in metal suggests that at an elevated temperature, the distribution of excess energy between the lattice and electronic subsystem maintains the local equilibrium of electron distribution via electron-phonon coupling, which affects the FWHM of phonon modes. The renormalization of a phonon mode due to this coupling scheme can be estimated from Allen's formulation [72,73], which states $\Delta\Gamma \propto \lambda \ \Delta N(E_F)$, where $\Delta N(E_F)$ and $\Delta\Gamma$ are the changes in the density of electronic states at the Fermi level and the corresponding change in linewidth of the phonon mode, respectively; λ is the electron-phonon coupling constant.

We look into the variation of Raman spectral width with temperature, as obtained by analyzing Raman spectra recorded at various temperatures. The evolution of full width at half maximum (FWHM) for the same three phonon modes, P1, P3, and P5, discussed in Fig. 3, are plotted in Fig. 5(a). Due to the increase in anharmonicity in the vibrational potential with the rise in temperature, FWHM increases with temperature monotonically following the relation [57]

$$\Gamma(T) = C\left(1 + \frac{2}{e^{\Phi/2} - 1}\right)$$
$$+ D\left(1 + \frac{3}{e^{\Phi/3} - 1} + \frac{3}{(e^{\Phi/3} - 1)^2}\right). \quad (2)$$

C and D are anharmonicity coefficients corresponding to three- and four-phonon decay processes. We fitted the full range of experimental data points in Fig. 5(a) using Eq. (2). The best fits to the data points in all panels are shown by red solid lines in Fig. 5(a). Raman wave number and FWHM are governed by the real and imaginary components of the self-energy of the phonon due to electron-phonon interaction. Reports in the literature [74,75] suggest that in strongly correlated systems, the imaginary component of phonon self-energy is less affected by electron-phonon interaction, unlike
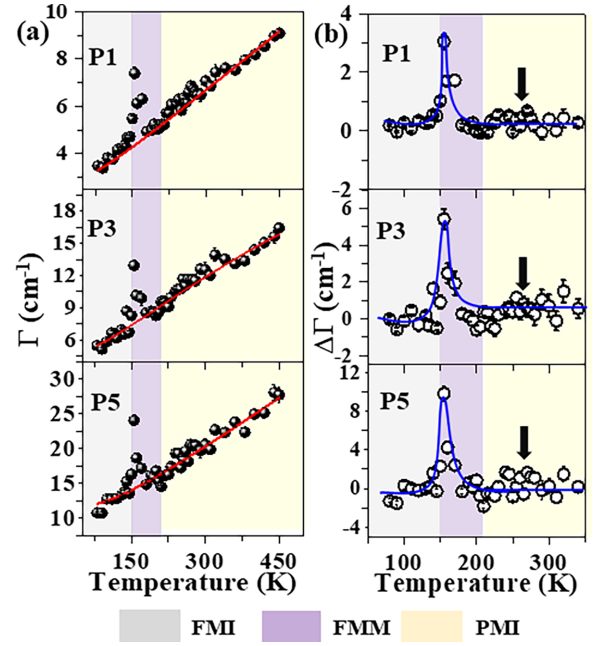
FIG. 5. (a) Change in linewidth (FWHM) of the Raman modes P1, P3, and P5 of O-LSMO, with temperature. The error bars are the standard deviation of the parameters as obtained from the fitting procedure. The solid red curves are the best fits to the data points using Eq. (2). (b) The variation of $\Delta\Gamma$ (obtained by subtracting the fitted values from the corresponding experimental data points at a given temperature) with temperature. In (a) and (b), the yellow, violet, and gray shaded areas mark the data points above T_{C2}^{OR}, between T_{C2}^{OR} and T_{C3}^{OR}, and below T_{C3}^{OR}, respectively. In (b) the temperature corresponding to T_{C1}^{OR} is marked by black down arrows.

its real part. We believe that possibly because of this reason, unlike Raman shift, the FWHM of Raman modes over the entire range of temperature of interest could be fitted using Eq. (2), which considers only the anharmonic contribution to phonon linewidth. However, the systematic mismatch between the fitted curves and the data points near the crossover between the FMM (violet-shaded area) and FMI (gray-shaded area) phases in all panels in Fig. 5(a) is noteworthy. We subtracted the values on the fitted curve from the measured data points at all temperatures for each mode and show as $\Delta\Gamma$ vs T plot in Fig. 5(b). An interesting trend is observed. There is an increase in $\Delta\Gamma$ as the system enters from the FMM to FMI phase (at the junction of gray- and violet-shaded regions) in Fig. 5(b). Following Allen's formalism, the sharp rise in $\Delta\Gamma$ in the metallic region and then its fall when the system enters into an insulating phase at T_{C3}^{OR} in Fig. 5 reflects a strong electron-phonon coupling at the FMI-FMM crossover in LSMO-0.125.

We recall the observations from ARPES on tetragonal-LSMO [71], which show a kink at $k \sim 0$ near Fermi energy in the momentum distribution curves and attribute this feature to quasiparticle-phonon coupling. In our observation in Fig. 5, the low wave-number gamma-point phonon modes are possibly picking up this characteristic of the electronic density of states of the FMM phase just before the present system of O-LSMO enters into the polaronic insulating
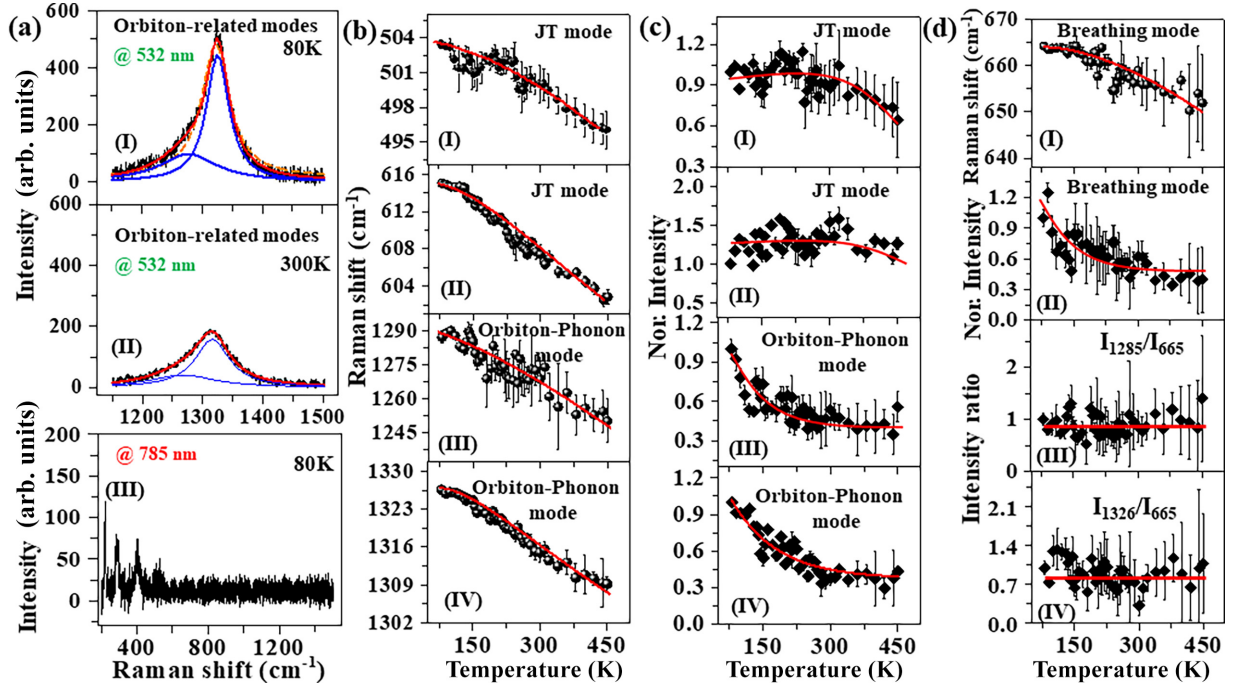
FIG. 6. (a) Raman spectrum of LSMO-0.125 recorded (I) at 80 K using 532 nm as the excitation wavelength; (II) at 300 K using the same wavelength; and (III) at 80 K using 785 nm as the excitation wavelength. In all panels measured data points are shown by black curves. In (I) and (II), deconvoluted components and net-fitted spectrum with two Lorentzian functions are shown by blue and red solid curves, respectively. Net-fitted spectrum with a single Lorentzian function is shown by an orange dashed curve in (I). (b) Variation in peak positions with temperature of (I) and (II) of the JT modes and (III) and (IV) of the orbiton-related phonon modes. The solid lines are the guide to the eyes. (c) Variation in normalized (with respect to the value at 80 K) intensities with temperature of (I) and (II) of the JT modes and (III) and (IV) of the orbiton-related modes. (d) Evolution of (I) Raman shift and (II) intensity of the breathing mode at 665 cm^{-1} with temperature. The intensity ratios of the orbiton-related modes at 1285 and 1326 cm^{-1} to that of the breathing mode are shown in panels (III) and (IV).

phase (refer to later discussion). Interestingly, in the case of R-LSMO-0.175, which does not exhibit low-temperature MIT, data points over the entire range of temperature could be fitted fairly well with Eq. (2) (see Fig. S6 in Ref. [33]). The above discussion further indicates the probable crucial role of structural symmetry in determining electron-phonon coupling in the system. The lack of knowledge on the variation of $\Delta N(E_F)$ with temperature refrained us from the quantitative estimation λ.

C. Coupling of orbital polaron and the phonon in the FMI phase

Next, through a brief discussion, we confirm the existence of orbital polaron in the FMI phase of the present system O-LSMO (LSMO-0.125). As mentioned earlier, extensive discussions on higher-order Raman modes to demonstrate the existence of orbital polaron in the FMI phase of O-LSMO are available in the literature [23–28]. Our observations in LSMO-0.125 reiterate the same. Refer to the intense high wavenumber Raman mode between 1150 and 1500 cm^{-1} in Fig. 2(a). Due to the higher intensity of the observed high wave-number features in Fig. 2(a), we rule out the possibility of their origin as the overtone of the first-order Raman modes [28].

Quite a few articles in the literature [24,28] indicated high wave-number Raman modes with an excitation wavelength of ~2 eV carry the signature of orbital ordering in LaMnO$_3$

and low hole-doped LSMO. Figures 6(a.I) and 6(a.II) plot Raman spectra of LSMO-0.125 over 1150 and 1500 cm^{-1} at 80 and 300 K recorded using 532 nm (~2.33 eV, close to the orbiton excitation energy of LSMO [24,28]) as the excitation wavelength. As a single Lorentzian function could not fit the data points [refer to the dashed curve in Fig. 6(a.I)] satisfactorily, we deconvoluted the spectral range between 1150 and 1500 cm^{-1} with two Lorentzian functions. The fitted peak positions for these two modes are 1285 and 1326 cm^{-1}. Raman spectrum recorded at 300 K using the same excitation wavelength is shown in Fig. 6(a.II). The intensity of both peaks drops with temperature. It is to be noted that the spectrum recorded at 80 K for the compound with 785 nm as the excitation wavelength over the spectral range between 200 and 1500 cm^{-1} [Fig. 6(a.III)] does not exhibit the high wave-number modes, confirming the orbiton resonance phenomenon. Thus, we assign both spectral features at 1285 and 1326 cm^{-1} in Fig. 6(a.I) to orbiton-related phonon mode in the system.

Further, we look into the possible origins of these modes in LSMO-0.125. Figures 6(b.I) and 6(b.II) plot the change in Raman shift of the peaks at 503 and 615 cm^{-1} with temperature. Both these modes are related to JT distortion in the system [23,24,76,77]. It is to be noted that though the cooperative JT distortion sets in only at T_{C1}^{OR}, the dynamical JT distortion can exist much beyond this temperature [78]. JT phonon modes are affected by locally deformed

octahedra and dynamically disordered octahedra. We observe a softening of the modes by $\sim$8 and 12 cm^{-1} over the entire temperature range for these two JT modes, respectively. We do not observe any anomalous softening of the JT modes across the magnetic phase transition temperature and at T_{C1}^{OR}. Unlike these modes, both orbiton-related modes undergo an unusually large change ($\sim$20–40 cm^{-1}) in wave number with temperature [Figs. 6(b.III) and 6(b.IV)]. The intensities of both JT modes remain unaffected by the rise in temperature up to 260 K (T_{C1}^{OR}) and then slightly drop down [Figs. 6(c.I) and 6(c.II)], as beyond this temperature, only dynamical distortion contributes. However, the intensity of both high wave-number modes drops monotonously with temperature [Figs. 6(c.III) and 6(c.IV)] over this temperature range.

Reports in the literature suggest that orbiton-polarons, the genesis of which are dressed electrons by orbitals, give rise to the low-temperature dominating FMI phase in this compound [23,79,80]. The orbiton-polarons couple with the breathing mode [79,80] of LSMO. Figures 6(d.I) and 6(d.II) plot the variation in peak position and intensity of the observed breathing mode at 665 cm^{-1} with temperature. We find a monotonic softening of this mode by 15 cm^{-1} with the increase in temperature. It is to be noted that in Fig. 6(d.I), the drop in the peak position is much higher than the same for first-order Raman modes. In Fig. 6(d.II), we find that the intensity of this mode drops monotonically with temperature, and its nature is very similar to that of orbiton-related modes shown in Figs. 6(c.III) and 6(c.IV). Figures 6(d.III) and 6(d.IV) plot the intensity ratio of both orbiton-related modes and the breathing mode. Due to the drop in intensities of both modes at high temperatures, the error bars to the data points for the ratio are large above 300 K. Within this error in measurements, the ratio remains nearly unchanged with temperature. An interesting aspect to note here is that with 785 nm as the excitation wavelength in Fig. 6(a.III), both higher-order orbiton-related phonon mode and the breathing mode are not observed. The above results suggest that the higher-order orbiton-related modes possibly arise due to the coupling of the orbiton-polaron with the phonon. The same claim was made earlier in the literature from more detailed Raman measurements [23,24]. In the case of LSMO-0.175, despite the presence of JT broad mode at 500 cm^{-1}, we do not observe any signature of the higher wave-number orbiton-related Raman signature in LSMO-0.175. This further supports the fact that JT distortion is not the sole origin of orbital ordering and FMI phase in LSMO, as we claimed from our observations in LSMO-0.125 (Fig. 6).

V. SUMMARY

We explore the role of phonons in multiple magnetic and electric phase transitions of the perovskite manganite orthorhombic LSMO-0.125 and rhombohedral LSMO-0.175. Micro-Raman measurements over a wide range of temperatures, encompassing the various magnetic and electrical phases of the system, are carried out. The observed anomalous changes in Raman shift across the transition temperatures indicate an intricate nature of spin-phonon coupling mechanisms, involving various types of spin-spin interactions in the system. A unique undulation of Raman shift with temperature is observed in the regime over which the systems are expected to attain a stripe magnetic texture. It is to be noted that the physics of microscopic mechanisms involved in complex spin-phonon coupling following the Hamiltonian, which involves both isotropic and anisotropic interactions, are still not fully understood. We hope our detailed experimental results will motivate researchers for further theoretical studies to investigate the phonon anomalies in such cases quantitatively. Further, the analysis of Raman linewidth suggests a strong electron-phonon coupling near the Fermi surface at the low-temperature MIT in the FM phase of LSMO-0.125. Wavelength- and temperature-dependent Raman measurements and detailed spectral analysis of the JT mode and breathing mode confirm the expected signature of orbiton-polaron in the FMI phase of O-LSMO.

ACKNOWLEDGMENTS

[1] H. Kawano, R. Kajimoto, R. M. Kubota, and H. Yoshizawa, Canted antiferromagnetism in an insulating lightly doped La$_{1-x}$Sr$_x$MnO$_3$ with x $\leqslant$ 0.17, Phys. Rev. B **53**, 2202 (1996).

[2] J. S. Zhou, J. B. Goodenough, A. Asamitsu, and Y. Tokura, Pressure-induced polaronic to itinerant electronic transition in La$_{1-x}$Sr$_x$MnO$_3$ crystals, Phys. Rev. Lett. **79**, 3234 (1997).

[3] H. Fujishiro, M. Ikebe, and Y. Konno, Phase transition to antiferromagnetic state in La$_{1-x}$Sr$_x$MnO$_3$ ($x \geqslant 0.5$), J. Phys. Soc. Jpn. **67**, 1799 (1998).

[4] B. Dabrowski, X. Xiong, Z. Bukowski, R. Dybzinski, P. W. Klamut, J. E. Siewenie, O. Chmaissem, J. Shaffer, C. W. Kimball, J. D. Jorgensen, and S. Short, Structure-properties phase diagram for La$_{1-x}$Sr$_x$MnO$_3$ ($0.1 < x < 0.2$), Phys. Rev. B **60**, 7006 (1999).

[5] J. Hemberger, A. Krimmel, T. Kurz, H. A. Krug von Nidda, V. Y. Ivanov, A. A. Mukhin, A. M. Balbashov, and A. Loidl, Structural, magnetic, and electrical properties of single-crystalline $La_{1-x}Sr_xMnO_3$ ($0.4 < x < 0.85$), Phys. Rev. B **66**, 094410 (2002).

[6] O. Chmaissem, B. Dabrowski, S. Kolesnik, J. Mais, J. D. Jorgensen, and S. Short, Structural and magnetic phase diagrams of $La_{1-x}Sr_xMnO_3$ and $Pr_{1-Y}Sr_yMnO_3$, Phys. Rev. B **67**, 094431 (2003).

[7] A. Szewczyk, M. Gutowska, and B. Dabrowski, Specific heat and phase diagram of heavily doped $La_{1-x}Sr_xMnO_3$ ($0.45 < x < 1.0$), Phys. Rev. B **72**, 224429 (2005).

[8] J. K. Tiwari, H. C. Chauhan, B. Kumar, and S. Ghosh, 3D-Ising like ferromagnetism in skyrmionic bubbles host infinite-layer $La_{0.825}Sr_{0.175}MnO_3$ manganite perovskite, J. Phys.: Condens. Matter **32**, 195803 (2020).

[9] H. Chen, D. Zheng, Y. Wang, P. Wang, C. Jin, Z. Li, and H. Bai, Secondary insulator-to-metal transition and magnetic properties in epitaxial $La_{0.92}Sr_{0.08}MnO_3$ films, Phys. Rev. B **106**, 064103 (2022).

[10] A. Urushibara, Y. Moritomo, T. Arima, A. Asamitsu, G. Kido, and Y. Tokura, Insulator-metal transition and giant magnetoresistance in $La_{1-x}Sr_xMnO_3$, Phys. Rev. B **51**, 14103 (1995).

[11] Y. Moritomo, A. Asamitsu, H. Kuwahara, and Y. Tokura, Giant magnetoresistance of manganese oxides with a layered perovskite structure, Nature (London) **380**, 141 (1996).

[12] M. Viret, M. Drouet, J. Nassar, J. P. Contour, C. Fermon, and A. Fert, Low-field colossal magnetoresistance in manganite tunnel spin valves, EPL **39**, 545 (1997).

[13] X. Hong, A. Posadas, A. Lin, and C. H. Ahn, Ferroelectric-field-induced tuning of magnetism in the colossal magnetoresistive oxide $La_{1-x}Sr_xMnO_3$, Phys. Rev. B **68**, 134415 (2003).

[14] X. Y. Wang, C. Jin, P. Wang, X. Pang, W. C. Zheng, D. X. Zheng, Z. Q. Li, R. K. Zheng, and H. L. Bai, Defects induced huge magnetoresistance in epitaxial $La_{1-x}Sr_xMnO_3$ thin films deposited by magnetic sputtering, Appl. Phys. Lett. **115**, 182405 (2019).

[15] P. Salev, L. Fratino, D. Sasaki, S. Bag, Y. Takamura, M. Rozenberg, and I. K. Schuller, Magnetoresistance anomaly during the electrical triggering of a metal-insulator transition, Phys. Rev. B, **108**, 174434 (2023).

[16] A. Kotani, H. Nakajima, Y. Ishii, K. Harada, and S. Mori, Observation of spin textures in $La_{1-x}Sr_xMnO_3$ ($x = 0.175$), AIP Adv. **6**, 056403 (2016).

[17] A. Kotani, H. Nakajima, K. Harada, Y. Ishii, and S. Mori, Lorentz microscopy and small-angle electron diffraction study of magnetic textures in $La_{1-x}Sr_xMnO_3$ ($0.15 < x < 0.30$): The role of magnetic anisotropy, Phys. Rev. B **94**, 024407 (2016).

[18] A. Kotani, H. Nakajima, K. Harada, Y. Ishii, and S. Mori, Field-temperature phase diagram of magnetic bubbles spanning charge/orbital ordered and metallic phases in $La_{1-x}Sr_xMnO_3$ ($x = 0.125$), Phys. Rev. B **95**, 144403 (2017).

[19] J. Fan, Y. Xie, Y. Zhu, F. Qian, Y. Ji, D. Hu, and H. Yang, Emergent phenomena of magnetic skyrmion and large DM interaction in perovskite manganite $La_{0.8}Sr_{0.2}MnO_3$, J. Magn. Magn. Mater. **483**, 42 (2019).

[20] Y. Zhang, J. Liu, Y. Dong, S. Wu, J. Zhang, J. Wang, and J. Zhang, Strain-driven Dzyaloshinskii-Moriya interaction for room-temperature magnetic skyrmions, Phys. Rev. Lett. **127**, 117204 (2021).

[21] M. Bowen, M. Bibes, A. Barthélémy, J. P. Contour, A. Anane, Y. Lemaître, and A. Fert, Nearly total spin polarization in $La_{2/3}Sr_{1/3}MnO_3$ from tunneling experiments, Appl. Phys. Lett. **82**, 233 (2003).

[22] E. Saitoh, S. Okamoto, K. T. Takahashi, K. Tobe, K. Yamamoto, T. Kimura, S. Ishihara, S. Maekawa, and Y. Tokura, Observation of orbital waves as elementary excitations in a solid, Nature (London) **410**, 180 (2001).

[23] K. Y. Choi, P. Lemmens, T. Sahaoui, G. Güntherodt, Y. G. Pashkevich, V. P. Gnezdilov, and A. Revcolevschi, Existence of orbital polarons in ferromagnetic insulating $La_{1-x}Sr_xMnO_3$ ($0.11 \leqslant x \leqslant 0.14$) revealed by giant phonon softening, Phys. Rev. B **71**, 174402 (2005).

[24] K. Y. Choi, P. Lemmens, G. Güntherodt, Y. G. Pashkevich, V. P. Gnezdilov, P. Reutler, L. Pinsard-Gaudart, B. Büchner, and A. Revcolevschi, Orbiton-mediated multiphonon scattering in $La_{1-x}Sr_xMnO_3$, Phys. Rev. B **72**, 024301 (2005).

[25] P. B. Allen and V. Perebeinos, Anti-Jahn-Teller polaron in $LaMnO_3$, Phys. Rev. B **60**, 10747 (1999).

[26] P. B. Allen and V. Perebeinos, Self-trapped excitation, and Franck-Condon spectra predicted in $LaMnO_3$, Phys. Rev. Lett. **83**, 4828 (1999).

[27] V. Perebeinos and P. B. Allen, Multiphonon resonant Raman scattering predicted in $LaMnO_3$ from the Franck-Condon process via self-trapped excitons, Phys. Rev. B **64**, 085118 (2001).

[28] R. Krüger, B. Schulz, S. Naler, R. Rauer, D. Budelmann, J. Bäckström, K. H. Kim, S.-W. Cheong, V. Perebeinos, and M. Rübhausen, Orbital ordering in $LaMnO_3$ investigated by resonance Raman spectroscopy, Phys. Rev. Lett. **92**, 097203 (2004).

[29] B. Kumar, H. C. Chauh, A. Baro, J. Saini, A. Tiwari, M. Verma, Y. Bitla, and S. Ghosh, Origin of magnetic anisotropy in $La_{1-x}Sr_xMnO_3$, arXiv:2305.16493.

[30] L. Pinsard, J. Rodríguez-Carvajal, A. H. Moudden, A. Anane, A. Revcolevschi, and C. Dupas, Jahn-Teller effect and ferromagnetic ordering in $La_{0.875}Sr_{0.125}MnO_3$: A reentrant behaviour, Phys. B: Condens. Matter **234**, 856 (1997).

[31] J. V. Brink, Orbital excitations in $LaMnO_3$, Phys. Rev. Lett. **87**, 217202 (2001).

[32] J. Geck, P. Wochner, S. Kiele, R. Klingeler, A. Revcolevschi, M. Zimmermann, and P. Reutler, Orbital order-induced ferromagnetic insulating properties, New J. Phys. **6**, 152 (2004).

[33] See Supplemental Material at http://link.aps.org/supplemental/10.1103/PhysRevB.109.214411 for: S1. Rietveld refined XRD patterns of LSMO-0.125 and LSMO-0.175 with space group Pbnm and R-3C; S2. Temperature-dependent Raman spectra; S3. DFT calculations of Raman modes; S4. Tables listing the values of anharmonic coefficients A and B in Eq. (1) for Figs. 3 and 4, and C and D in Eq. (2) for Fig. 5 for all modes discussed for LSMO-0.125 and LSMO-0.175; S5. Evolution of Raman shifts with temperature for independent measurements; and S6. Variation of Raman linewidth with temperature for LSMO-0.175.

[34] M. Iliev and M. Abrashev, Raman spectroscopy of orthorhombic perovskitelike $YMnO_3$ and $LaMnO_3$, Phys. Rev. B **57**, 2872 (1998).

[35] V. B. Podobedov, A. Weber, D. B. Romero, J. P. Rice, and H. D. Drew, Effect of structural and magnetic transitions in $La_{1-x}M_xMnO_3$ (M = Sr, Ca) single crystals Raman scattering, Phys. Rev. B **58**, 43 (1998).

[36] E. Granado, N. O. Moreno, A. Garcia, J. A. Sanjurjo, C. Rettori, and I. Torriani, Phonon Raman scattering in $R_{1-x}A_xMnO_{3+d}$. (R = La, Pr; A = Ca,Sr), Phys. Rev. B **58**, 11435 (1998).

[37] W. Reichardt and M. Braden, Anomalous features in the bond stretching vibrations of $La_{1-x}Sr_xMnO_3$, Phys. B: Condens. Matter **263**, 416 (1999).

[38] M. N. Iliev and M. V. Abrashev, Raman phonons and Raman Jahn–Teller bands in perovskite maganites, J. Raman Spectrosc. **32**, 805 (2001).

[39] M. N. Iliev, V. G. Hadjiev M, A. P. Litvinchuk, F. Yen, Y. Q. Wang, Y. Y. Sun, and M. M. Gospodinov, Multiple-order Raman scattering from rare-earth manganites: Oxygen isotope and rare-earth substitution effects, Phys. Rev. B **75**, 064303 (2007).

[40] P. Gianozzi, S. Baroni, N. Bonini, and R. M. Wentzcovitch, Quantum Espresso: A modular and open-source software project for quantum simulations of materials, J. Phys.: Condens. Matter **21**, 395502 (2009).

[41] P. Giannozzi, O. Andreussi, T. Brumme, and S. Baroni, Advanced capabilities for materials modeling with Quantum Espresso, J. Phys.: Condens. Matter **29**, 465901 (2017).

[42] P. Giannozzi, O. Baseggio, P. Bonfà, and S. Baroni, Quantum Espresso toward the exascale, J. Chem. Phys. **152**, 154105 (2020).

[43] A. Floris, I. Timrov, B. Himmetoglu, N. Marzari, S. de Gironcoli, and M. Cococcioni, Hubbard-corrected density functional perturbation theory with ultrasoft pseudopotentials, Phys. Rev. B **101**, 064305 (2020).

[44] H. J. Monkhorst and J. D. Pack, Special points for Brillouin-zone integrations, Phys. Rev. B **13**, 5188 (1976).

[45] J. P. Perdew, K. Burke, and M. Ernzerhof, Generalized gradient approximation made simple, Phys. Rev. Lett. **77**, 3865 (1996).

[46] G. Trimarchi and N. Binggeli, Structural and electronic properties of $LaMnO_3$ under pressure: An ab initio LDA+ U study, Phys. Rev. B **71**, 035101 (2005).

[47] A. L. Gavin, W. Graeme, and S. Watson, Modelling the electronic structure of orthorhombic $LaMnO_3$, Solid State Ionics **299**, 13 (2017).

[48] S. Satpathy, Z. S. Popović, and F. R. Vukajlović, Electronic structure of the perovskite oxides: $La_{1-x}Ca_xMnO_3$, Phys. Rev. Lett. **76**, 960 (1996).

[49] R. Fletcher, *Practical Methods of Optimization*, 2nd ed. (Wiley, Chichester, 1987).

[50] N. Marzari, D. Vanderbilt, A. De Vita, and M. C. Payne, Thermal contraction and disordering of the Al (110) surface, Phys. Rev. Lett. **82**, 3296 (1999).

[51] I. Timrov, F. Aquilante, L. Binci, M. Cococcioni, and N. Marzari, Erratum: Pulay forces in density-functional theory with extended Hubbard functionals: From nonorthogonalized to orthogonalized manifolds, Phys. Rev. B **105**, 199901(E) (2022).

[52] I. Pallikara, P. Kayastha, J. M. Skelton, and L. D. Whalley, The physical significance of imaginary phonon modes in crystals, Electron. Struct. **4**, 033002 (2022).

[53] R. Islam, S. P. Madsen, and M. Christensen, Exploring the magnetic properties of W-type $SrFe_{18}O_{27}$ hexaferrite: Insights from a first-principles study, Phys. Rev. B **109**, 024414 (2024).

[54] E. Granado, A. García, J. A. Sanjurjo, C. Rettori, I. Torriani, F. Prado, R. D. Sánchez, A. Caneiro, and S. B. Oseroff, Magnetic ordering effects in the Raman spectra of $La_{1-x}Mn_xO_3$, Phys. Rev. B **60**, 11879 (1999).

[55] P. G. Radaelli and S. W. Cheong, Structural phenomena associated with the spin-state transition in $LaCoO_3$, Phys. Rev. B **66**, 094408 (2002).

[56] C. Ritter, M. R. Ibarra, J. M. De Teresa, P. A. Algarabel, C. Marquina, J. Blasco, and S. W. Cheong, Influence of oxygen content on the structural, magnetotransport, and magnetic properties of $LaMnO_{3+\delta}$, Phys. Rev. B **56**, 8902 (1997).

[57] M. Balkanski, R. F. Wallis, and E. Haro, Anharmonic effects in light scattering due to optical phonons in silicon, Phys. Rev. B **28**, 1928 (1983).

[58] K. Y. Choi, P. Lemmens, G. Guntherodt, M. Pattabiraman, G. Rangarajan, V. P. Gnezdilov, G. Balakrishnan, D. M. Paul, and M. R. Lees, Raman scattering study of $Nd_{1-x}Sr_xMnO_3$ ($x = 0.3, 0.5$), J. Phys.: Condens. Matter **15**, 3333 (2003).

[59] J. Son, B. C. Park, C. H. Kim, H. Cho, S. Y. Kim, L. J. Sandilands, C. Sohn, J. G. Park, S. J. Moon, and T. W. Noh, Unconventional spin-phonon coupling via the Dzyaloshinskii–Moriya interaction, npj Quantum Mater. **4**, 17 (2019).

[60] T. Moriya, New mechanism of anisotropic superexchange interaction, Phys. Rev. Lett. **4**, 228 (1960).

[61] T. Moriya, Anisotropic superexchange interaction and weak ferromagnetism, Phys. Rev. **120**, 91 (1960).

[62] S. Chandra, A. Biswas, S. Datta, B. Ghosh, A. K. Raychaudhuri, and H. Srikanth, Inverse magnetocaloric and exchange bias effects in single crystalline $La_{0.5}Sr_{0.5}MnO_3$ nanowires, Nanotechnology **24**, 505712 (2013).

[63] P. Dore, P. Postorino, A. Sacchetti, M. Baldini, R. Giambelluca, M. Angeloni, and G. Balestrino, Raman measurements on thin films of the $La_{0.7}Sr_{0.3}MnO_3$ manganite: A probe of substrate-induced effects, Eur. Phys. J. B **48**, 255 (2005).

[64] J. Wang, H. Dong, and S. W. Li, Magnetic dipole-dipole interaction induced by the electromagnetic field, Phys. Rev. A **97**, 013819 (2018).

[65] Y.-D. Chuang, A. D. Gromko, D. S. Dessau, T. Kimura, and Y. Tokura, Fermi surface nesting and nanoscale fluctuating charge/orbital ordering in colossal magnetoresistive oxides, Science **292**, 1509 (2001).

[66] N. Mannella, W. L. Yang, X. J. Zhou, H. Zheng, J. F. Mitchell, J. Zaanen, T. P. Devereaux, N. Nagaosa, Z. Hussain, and Z.-X. Shen, Nodal quasiparticle in pseudogapped colossal magnetoresistive manganites, Nature (London) **438**, 474 (2005).

[67] Z. Sun, Y.-D. Chuang, A. V. Fedorov, J. F. Douglas, D. Reznik, F. Weber, N. Aliouane, D. N. Argyriou, H. Zheng, J. F. Mitchell, T. Kimura, Y. Tokura, A. Revcolevschi, and D. S. Dessau, Quasiparticle-like peaks, kinks, and electron-phonon coupling at the (π, 0) regions in the CMR oxide $La_{2-2x}Sr_{1+2x}Mn_2O_7$, Phys. Rev. Lett. **97**, 056401 (2006).

[68] Z. Sun, J. F. Douglas, A. V. Fedorov, Y.-D. Chuang, H. Zheng, J. F. Mitchell, and D. S. Dessau, A local metallic state in globally insulating $La_{1.24}Sr_{1.76}Mn_2O_7$ well above the metal–insulator transition, Nat. Phys. **3**, 248 (2007).

[69] S. de Jong, Y. Huang, I. Santoso, F. Massee, R. Follath, O. Schwarzkopf, L. Patthey, M. Shi, and M. S. Golden, Quasiparticles and anomalous temperature dependence of the low-lying states in the colossal magnetoresistant oxide $La_{2-2x}Sr_{1+2x}Mn_2O_7$ ($x = 0.36$) from angle-resolved photoemission, Phys. Rev. B **76**, 235117 (2007).

[70] F. Massee, S. de Jong, Y. Huang, W. K. Siu, I. Santoso, A. Mans, A. T. Boothroyd, D. Prabhakaran, R. Follath, A. Varykhalov, L. Patthey, M. Shi, J. B. Goedkoop, and M. S. Golden, Bilayer

manganites reveal polarons in the midst of a metallic breakdown, Nat. Phys. **7**, 978 (2011).

[71] K. Horiba, M. Kitamura, K. Yoshimatsu, M. Minohara, E. Sakai, M. Kobayashi, and H. Kumigashira, Isotropic kink and quasiparticle excitations in the three-dimensional perovskite manganite $La_{0.6}Sr_{0.4}MnO_3$, Phys. Rev. Lett. **116**, 076401 (2016).

[72] P. B. Allen, Effect of soft phonons on superconductivity: A reevaluation and a positive case for Nb3Sn, Solid State Commun. **14**, 937 (1974).

[73] P. B. Allen, Theory of thermal relaxation of electrons in metals, Phys. Rev. Lett. **59**, 1460 (1987).

[74] A. Thomas, P. Telang, K. Mishra, M. Cesnek, J. Bednarcik, D. V. S. Muthu, and A. K. Sood, Role of spin-phonon and electron-phonon interactions in the phonon renormalization of $(Eu_{1-x}Bi_x)_2Ir_2O_7$ across the metal-insulator phase transition: Temperature-dependent Raman and x-ray studies, Phys. Rev. B **105**, 075145 (2022).

[75] P. S. Patnaik, A. Kumar, A. Roy, and S. M. Yusuf, Intertwined spin and phonon correlations across the magnetic compensation

temperature in magnetoelectric $Li_{0.5}Fe_{2.5-x}Cr_xO_4$, Phys. Rev. B **108**, 014438 (2023).

[76] M. N. Iliev, M. V. Abrashev, J. Laverdière, S. Jandl, M. M. Gospodinov, Y. Q. Wang, and Y. Y. Sun, Distortion-dependent Raman spectra and mode mixing in $RMnO_3$ perovskites (R = La, Pr, Nd, Sm, Eu, Gd, Tb, Dy, Ho, Y), Phys. Rev. B **73**, 064302 (2006).

[77] S. Merten, V. Bruchmann-Bamberg, B. Damaschke, K. Samwer, and V. Moshnyaga, Jahn-Teller reconstructed surface of the doped manganites shown by means of surface-enhanced Raman spectroscopy, Phys. Rev. Mater, **3**, 060401(R) (2019).

[78] L. Martín-Carrón and A. De Andrés, Melting of the cooperative Jahn-Teller distortion in $LaMnO_3$ single crystal studied by Raman spectroscopy, Eur. Phys. J. B **22**, 11 (2001).

[79] R. Kilian and G. Khaliullin, Orbital polarons in the metal-insulator transition of manganites, Phys. Rev. B **60**, 13458 (1999).

[80] T. Mizokawa, D. I. Khomskii, and G. A. Sawatzky, Orbital polarons and ferromagnetic insulators in manganites, Phys. Rev. B **63**, 024403 (2000).